



Swansea University  
Prifysgol Abertawe



## Cronfa - Swansea University Open Access Repository

---

This is an author produced version of a paper published in:

*Nanoscale*

Cronfa URL for this paper:

<http://cronfa.swan.ac.uk/Record/cronfa51571>

---

### Paper:

Minakshi, M., Mitchell, D., Munnangi, A., Barlow, A. & Fichtner, M. (2018). New insights into the electrochemistry of magnesium molybdate hierarchical architectures for high performance sodium devices. *Nanoscale*, 10(27), 13277-13288.

<http://dx.doi.org/10.1039/C8NR03824D>

---

This item is brought to you by Swansea University. Any person downloading material is agreeing to abide by the terms of the repository licence. Copies of full text items may be used or reproduced in any format or medium, without prior permission for personal research or study, educational or non-commercial purposes only. The copyright for any work remains with the original author unless otherwise specified. The full-text must not be sold in any format or medium without the formal permission of the copyright holder.

Permission for multiple reproductions should be obtained from the original author.

Authors are personally responsible for adhering to copyright and publisher restrictions when uploading content to the repository.

<http://www.swansea.ac.uk/library/researchsupport/ris-support/>



**New insights into the electrochemistry of magnesium molybdate hierarchical architectures for high performance sodium devices**

Journal:	<i>Nanoscale</i>
Manuscript ID	NR-ART-05-2018-003824.R1
Article Type:	Paper
Date Submitted by the Author:	11-Jun-2018
Complete List of Authors:	Meenakshi, Manickam; Murdoch University, Chemistry Mitchell, David; University of Wollongong, Australian Institute for Innovative Materials Munnangi, Anji Reddy; Helmholtz Institute Ulm, Department of Materials Barlow, Anders; La Trobe University, Department of Chemistry and Physics Fichtner, Maximilian; Karlsruhe Institute of Technology, Institute of Nanotechnology

## **New insights into the electrochemistry of magnesium molybdate hierarchical architectures for high performance sodium devices**

**<sup>1,2</sup>Manickam Minakshi\*, <sup>3</sup>David R.G. Mitchell, <sup>2</sup>Anji Reddy Munnangi, <sup>4</sup>Anders J. Barlow and <sup>2</sup>Maximilian Fichtner\***

*<sup>1</sup>School of Engineering and Information Technology, Murdoch University, WA 6150, Australia*

*<sup>2</sup>Helmholtz Institute Ulm for Electrochemical Energy Storage (HIU), Ulm 89081, Germany*

*<sup>3</sup>Electron Microscopy Centre, Australian Institute for Innovative Materials, Innovation Campus, University of Wollongong, North Wollongong, NSW 2500, Australia*

*<sup>4</sup>Centre for Materials and Surface Science, La Trobe University, Bundoora, VIC 3086, Australia*

### **Abstract**

Magnesium molybdate ( $\text{MgMoO}_4$ ), which possesses synergistic features combining both hierarchical platelike nanomaterials and porous architectures, has been successfully synthesized through a facile combustion synthesis at a low temperature. The hierarchical architecture is characterized by X-ray diffraction (XRD), field emission scanning electron microscopy (FESEM), scanning transmission electron microscopy (TEM), and X-ray photoelectron spectroscopy (XPS) analyses. The as-obtained  $\text{MgMoO}_4$  nanoplates showed a porous structure with a pore-size distribution ranging from 50 to 70 nm. This porosity provides an electron transport pathway and enhanced surface reaction kinetics. The binding energies measured for Mg 2p, Mo 3d, 3p and O 1s are consistent with the literature, and with the metal ions being present as  $M$  (II) and  $M$  (VI) states, respectively. This indicates that the oxidation states of the metal cations are as-expected. The electrochemical behaviour of  $\text{MgMoO}_4$  was investigated using aqueous (NaOH) and non-aqueous solvents (NaClO<sub>4</sub> in EC:DMC: FEC) for supercapacitor and battery applications. The sodium-ion capacitor involves ion absorption and insertion into the  $\text{MgMoO}_4$  electrodes resulting in superior power and energy densities. However, the cycling stability was found to be stable only for an aqueous system. The formation of a solid electrolyte surface layer restricted the reversible capacity of the  $\text{MgMoO}_4$  in the sodium-battery. Nevertheless, it does offer some promise as an anode material for storing energy with high rate performance and excellent capacity retention. Detailed comparative analyses of various electrolytes in storage devices such as hybrid sodium-ion capacitors, sodium-ion batteries is vital for integration of hierarchical structured materials into practical applications. The reaction mechanisms are postulated.

E: [minakshi@murdoch.edu.au](mailto:minakshi@murdoch.edu.au); [m.fichtner@kit.edu](mailto:m.fichtner@kit.edu)

## Introduction

Today, the most significant global challenge is energy. It is reported that almost 80% of the world's energy consumption is from non-renewable sources.<sup>1</sup> Issues surrounding the use of fossil fuels and their environmental impacts have resulted in considerable interest in renewable energy. The intermittent nature of most forms of renewable energy (solar, wind, tidal) dictates that energy storage is a critical part of a reduced reliance on dispatchable sources of energy such as gas and coal. Batteries, supercapacitors, and hydrogen storage systems have great potential in efficient renewable energy storage.<sup>1,2</sup> Among different types of energy storage devices being examined, electrochemical energy storage devices are the most promising candidates.<sup>3-4</sup> Current technology rechargeable batteries based on lithium or sodium-ion are need to be optimized for storing renewable energy. This is due to relatively low power density and limited cyclability.<sup>5</sup>

One approach to improving energy storage technology involves combining elements of both batteries and capacitors, in a device termed a hybrid capacitor<sup>6</sup>. These deliver high energy and power density as well as reasonably long cycling stability with fast charging/discharging capabilities. However, hybrid capacitors deliver a much lower energy density compared to that of batteries.<sup>5-6</sup> Therefore, the current work has been focussed on the improvement of energy density via rational design of material and using a facile synthesis approach to obtain an electrode with the desired characteristics. Nanomaterials with a particle size distribution ranging from tens to hundreds of nanometers are found to be suitable for ion absorption, faster surface redox reaction, and ion storage.<sup>7</sup> In this work, we have developed and investigate a novel form of magnesium molybdate ( $\text{MgMoO}_4$ ), having both hierarchical architecture and a porous structure. The use of a porous electrode helps alleviate the internal stress created during rapid charging and discharging. The hierarchically porous material also offers high capacitance and a rapid ion transport owing to their low resistance to electrolyte

diffusion. This structure is likely to offer considerable advantages to the electrochemical performances in the molybdate family of materials. Combining such hierarchical structures to fabricate nanoplate electrodes might enable advanced materials with enhanced performance.

Various transition metal cations have been reported in the binary metal oxide framework  $\text{AMoO}_4$  ( $A =$  divalent metal ions; i.e. Mn, Co, and Ni).<sup>8-12</sup> The specific capacitance for the hybrid device of the nanostructured  $\text{MnMoO}_4$ <sup>10</sup>,  $\text{CoMoO}_4$ <sup>11</sup> and  $\text{NiMoO}_4$ <sup>12</sup> were reported to be around 20, 25 and 70  $\text{F g}^{-1}$  when performed in a two-electrode cell at 2  $\text{A g}^{-1}$  over 1000 cycles with voltage window of 1.6 V. However, the capacity retention of the  $\text{NiMoO}_4$  electrode is shown to deteriorate over multiple cycling.<sup>12-13</sup> Though binary metal oxide framework was used as electrode in lithium-ion battery but it is not widely reported for sodium system.

Herein, we report the synthesis and electrochemistry of magnesium molybdate ( $\text{MgMoO}_4$ ) hierarchical architectures obtained through a combustion route. We have assembled a hybrid capacitor based on  $\text{MgMoO}_4$  as the positive electrode and activated carbon as the negative electrode. Electrolytes tested included NaOH solution and non-aqueous solvent ( $\text{NaClO}_4$  in EC: DMC: FEC) separately. Many aqueous electrolytes such as acid, neutral and alkaline media have been explored as electrolytes in both batteries and supercapacitors. However, the corrosive nature of sulphate ions limit the cycle stability of the energy storage devices. Therefore, to have a meaningful comparison, NaOH has been chosen. To the best of our knowledge, there is no work reported on  $\text{MgMoO}_4$  for hybrid devices. We have tested and compared their performances in both aqueous and non-aqueous electrolytes. In both cases the specific capacitance was around 43  $\text{F g}^{-1}$ . The cell could be cycled reversibly in a voltage region of 1.6 V (aqueous) and 3.0 V (non-aqueous) but the capacitance retention is found to be excellent only for the aqueous system. In this aqueous case, plate like  $\text{MgMoO}_4$  exhibiting a capacitance 43  $\text{F g}^{-1}$  with an excellent cycling retention of over 95% in

1000 cycles is reported. In order to develop an alternative anode material, which can rival the hard carbon anode used in sodium-ion batteries, we extended our studies to test the feasibility of  $\text{MgMoO}_4$  in a battery using  $\text{MgMoO}_4$  as positive electrode and metallic sodium as the negative electrode. The preliminary results showed that  $\text{MgMoO}_4$  is suitable for high cycling stability with excellent retention (95% over 75 cycles) in discharge capacity. However, the storage capacity of  $225 \text{ mAh g}^{-1}$  need to be improved for practical applications. Our physical and electrochemical approaches provide understanding of the electrochemistry, the redox mechanism, the role of nanostructured electrode material and the type of electrolyte on the performance of this system. The charge-discharge mechanisms of  $\text{MgMoO}_4$  in the sodium-ion battery have also been postulated. The insights gained should enable us to further enhance and develop the storage capabilities of this type of system.

## **Experimental**

### ***Synthesis of magnesium molybdate***

Magnesium molybdate ( $\text{MgMoO}_4$ ) was synthesised using combustion process. All reagents were purchased from Sigma-Aldrich. In a typical synthesis, stoichiometric amounts of magnesium nitrate ( $\text{Mg}(\text{NO}_3)_2 \cdot 6\text{H}_2\text{O}$ ) in the presence of ammonium molybdate tetrahydrate ( $(\text{NH}_4)_6\text{Mo}_7\text{O}_{24} \cdot 4\text{H}_2\text{O}$ ) and urea ( $\text{CO}(\text{NH}_2)_2$ ) as a fuel were dissolved in de-ionised water (about 50 mL) with magnetic stirring. The pH of the solution was adjusted to 7 by drop wise addition of ammonia solution. Subsequently, the solution was evaporated on a heater overnight and moved to an oven at  $150 \text{ }^\circ\text{C}$  for 2 h for a complete dehydration of the precursors. Once dried, the dehydrated sample was transferred into a furnace at  $300 \text{ }^\circ\text{C}$  for 3 hours to transform the precursors to plate like  $\text{MgMoO}_4$  hierarchical architectures.

### ***Physical characterisation of $\text{MgMoO}_4$***

The phase purity of the as-synthesized sample was characterized by X-ray diffraction (XRD, Philips PANalytical, Bruker D8) analysis using  $\text{Cu-K}\alpha$  radiation at an accelerating voltage and current of 40 kV and 30 mA, respectively.

The morphology of the  $\text{MgMoO}_4$  material was characterized by Mira VP - Field Emission Scanning Electron Microscope (FESEM). The high-resolution imaging of the  $\text{MgMoO}_4$  material was carried out via scanning transmission electron microscopy (STEM) – imaging in various imaging modes: high angle annular dark field imaging (HAADF), bright field (BF) and secondary electron (SE) using a JEOL ARM 200F TEM operated at 200 kV. STEM specimens were prepared by grinding a small amount of powder in methanol and dispersing on a holey carbon film.

Brunauer, Emmett, and Tellet (BET) surface area measurements and porosity analysis were also carried out using a Micromeritics Tristar II surface area and porosity analyser. For porosity measurements, all samples were degassed at 100 °C overnight prior to analysis.

X-ray photoelectron spectra were acquired using a Kratos AXIS Nova instrument (Kratos Analytical Ltd, U.K.) equipped with a monochromated Al  $K\alpha$  radiation source (1486.69 eV) operating at 150 W power (15 kV, 10 mA). The source was operated at 150 W power (15 kV, 10 mA). Analysis chamber pressure was  $< 1 \times 10^{-9}$  Torr at the beginning of the analysis. High-resolution spectra acquired for selected photoemissions were recorded at 0.1 eV/step and a pass energy of 20 eV. The analysis area was approx. 300  $\mu\text{m}$  x 700  $\mu\text{m}$ . All spectra are calibrated by setting the main O 1s component position to 530.45 eV.

#### ***Electrochemical characterisation of $\text{MgMoO}_4$***

Electrolytes used were: aqueous 2M NaOH and non-aqueous, 1M  $\text{NaClO}_4$  in EC: DMC: FEC (88:10:2) for all supercapacitor and sodium-ion battery measurements. The hybrid device was constructed with  $\text{MgMoO}_4$  as the positive electrode and conventional activated carbon (AC) as the negative electrode. For the sodium-ion battery, metallic sodium (from Sigma Aldrich) was used as the anode.

For the three-electrode tests, a platinum wire of 10 cm length and 1 mm diameter and mercury–mercuric oxide (Hg/HgO) served as the counter and reference electrodes, respectively. For electrochemical measurements, the materials were investigated by

constructing a working electrode consisting of MgMoO<sub>4</sub> (or) activated carbon (70 wt. %), carbon black (20 wt.%), and poly-vinylidene fluoride (PVDF) binder (10 wt. %) with 0.4 mL of N-methyl-2-pyrrolidone (NMP) to make slurry. Ingredients were mixed in an agate mortar to produce a uniform paste, which was coated onto a 1 cm<sup>2</sup> graphite sheet / stainless steel disc as a current collector. Galvanostatic charge-discharge experiments and electrochemical impedance spectroscopy were performed using SP-150, Bio-Logic instrument and an Arbin battery testing unit (ARBIN BT-2000). Charge–discharge studies were carried out at a current density of 2 A g<sup>-1</sup> unless otherwise stated. All the measurements relating to the non-aqueous electrolyte involved a sealed Swagelok-type cell which was assembled in a glovebox under an Ar atmosphere and the analysis was then carried out in the air in a similar manner to that used for the aqueous system but with different negative electrode.

Specific capacitance and energy density of the hybrid device were calculated at the end of each charge-discharge test. Electrochemical impedance spectroscopy (EIS) was carried out with an amplitude of 5 mV over a frequency range of 10 mHz to 700 KHz at open circuit potential. The specific capacitance (SC) and energy density (E) of the device were calculated using the following equations:

$$SC \text{ (F g}^{-1}\text{)} = I \Delta t / m \Delta V \quad \text{Eq. (1)}$$

$$E \text{ (W h kg}^{-1}\text{)} = E = \frac{1}{2} SC \Delta V^2 \quad \text{Eq. (2)}$$

where  $SC$  is the specific capacitance (F g<sup>-1</sup>),  $I$  is the current (A) imposed to the cell for charge / discharge,  $\Delta t$  is the time taken to discharge in seconds (calculated from the discharge curves),  $m$  is the weight of the active electrode (MgMoO<sub>4</sub>) in g, and  $\Delta V$  is the voltage window (V). The discharge / charge capacities for the sodium battery were expressed in mAh/g.

For a hybrid cell, in order to maintain the charge conservation between the two electrodes, the mass ratio was calculated using the equation (3)



$$m^+ / m^- = (SC_- * \Delta V_-) / (SC_+ * \Delta V_+) \quad \text{Eq. (3)}$$

where  $m$  represents the mass in g.  $SC_-$  and  $SC_+$  represents the specific capacitance for the AC and  $MgMoO_4$ , respectively (calculated from Eq. 1);  $\Delta V_-$  and  $\Delta V_+$  the discharge/charge potential range for the AC and  $MgMoO_4$  electrodes, respectively.

The specific capacitance of the AC and  $MgMoO_4$  after subtracting from contributions of acetylene black and binder were calculated to be  $200 \text{ F g}^{-1}$  (for activated carbon) and  $125 \text{ F g}^{-1}$  (for  $MgMoO_4$ ). Based on the single electrode characteristics, from the above equation (3), the optimal mass ratio between AC and  $MgMoO_4$  was determined to be for a mass of 15 mg  $MgMoO_4$  material the mass of the AC was 5.62 mg.

## Results and Discussion

### *Physical characterization of platelike $MgMoO_4$ crystallites*

#### *(a) X-ray diffraction (XRD) studies*

The structure and phase purity of the as-synthesized  $MgMoO_4$  samples were examined by X-ray diffraction (Figure 1). All the diffraction peaks matched the standard XRD pattern of magnesium molybdate crystal (reported in JCPDS 021-0961,  $a = 10.281 \text{ \AA}$ ,  $b = 9.291 \text{ \AA}$ ,  $c = 7.030 \text{ \AA}$ ). The characteristic peaks located at different  $2\theta$  values were assigned to the respective planes as shown in Figure 1 and this confirms that chosen combustion synthesis at a low temperature ( $300 \text{ }^\circ\text{C}$ ) is sufficient to synthesise the  $MgMoO_4$  compound. No secondary phases or impurities were observed in the diffraction pattern. The broad diffraction peaks indicate the nanosized particles of the synthesized material. The obtained low signal to-noise ratio is not limited by the XRD itself but due to the chosen synthesis.

#### *(b) Field emission and transmission electron microscopy (FESEM and TEM) studies*

Scanning electron microscopy (SEM) and transmission electron microscopy (TEM) were employed to examine the morphology and structure of the as-synthesized  $MgMoO_4$

samples. Low magnification imaging (Fig. 2a), showed that the individual particles were fused into rounded clusters with a diameter of several microns with voids illustrating the formation of pores. High magnification imaging (Figs 2b-c), showed that individual particles consist of numerous plate-shaped particles of lengths up to a few nm with extensive porosity. The porosity most likely arises from the release of gases (like  $\text{NH}_3$ ,  $\text{CO}_2$ ) during the decomposition of precursors and urea as fuel through combustion synthesis. It is evident from SEM that clusters of  $\text{MgMoO}_4$  particles are closely connected to each other to form a continuous network-like structure that is a pre-requisite for an efficient utilization of active electrode material, eventually contributing to high storage. The corresponding elemental dispersive X-ray spectra (EDS in Fig. 2d) shows that the analysed area is mainly composed of Mg, Mo, C, and O.

Figures 3a-c show low magnification STEM images. The HAADF image in Fig. 3a shows contrast which is a function of thickness multiplied by atomic number squared. This produces very strong contrast between the molybdate phase and thin carbon support film. The BF image (Fig. 3b) shows diffraction contrast from the crystalline particles. However, the thickness of the largest clusters obscures the details of the individual crystallites. The SE image (Fig. 3c) shows the topographic structure of the particles – producing information analogous to that obtained from SE imaging in an SEM – albeit at much higher resolution. The  $\text{MgMoO}_4$  nanoparticles are associated with numerous pores and the pore sizes vary in several nanometers. Therefore, these three images (HAADF, BF, and SE) provide complementary structural insights. EDS mapping combined with phase analysis using principal component analysis (PCA), showed that the molybdate was a single phase – in agreement with XRD (Fig. S1). Figures 3d-f shows HAADF, BF and SE details of the region in Fig. 3a. It shows an ensemble of small plate-like crystals (of around 50 nm side length) stacked obliquely. These are clustered on the surface of larger  $\text{MgMoO}_4$  plates. The stacked

individual plate-like particles are clearly visible in Figs. 3h-i exhibiting a hierarchical architecture. High-resolution imaging of a thin plate appearance of around 10 nm (Fig. 3j) and a detail BF image (Fig. 3k) confirms the highly crystalline structure. The electron energy loss spectroscopy (EELS) analysis of this region shows (Fig. S2) small amount of carbon present in the molybdate framework. However, mottling in the HAADF image (Fig. 3j) and bright field contrast at lower magnification (Fig. 3l) reveals an extensive network of fine (ca 10nm) pores in the crystals.

The microscopy results show that a nanoplate-like  $\text{MgMoO}_4$  hierarchical architecture with considerable porosity has been successfully synthesized. The electrochemical performance of material is heavily influenced by the pore size distribution, therefore, the porosity of the  $\text{MgMoO}_4$  samples was measured by the Brunauer-Emmett-Teller (BET) and Barrett-Joyner-Halenda (BJH) analyses and the results are shown in Fig. 4. The samples possess well-developed porosity, reflected by the  $\text{N}_2$  sorption isotherm of type III,<sup>14</sup> having a BET surface area of  $25.2 \text{ m}^2\text{g}^{-1}$ . From the adsorption branch BJH method the porous structure consists of two main pore size distributions. This hierarchical structure consists of large pores, with a pore size range between 50 and 70 nm and on the walls of these pores are much smaller pores of around 10 nm. The hierarchical pores structure is likely to be high advantageous to electrochemical performance of the resulting electrode since it will facilitate the ion diffusion rate.<sup>15-17</sup>

### *(c) X-ray photoelectron spectroscopy (XPS) studies*

To ascertain the electronic state of the  $\text{MgMoO}_4$  sample, X-ray photoelectron spectroscopy (XPS) study was carried out and the results are shown in Fig. 5. XPS is a surface technique, the photoelectrons emitted from the sample surface have a kinetic energy that is specific to the element from which they originate, and the local bonding environment. Therefore, the signals indicate elemental composition and electronic (oxidation) state information. The wide

scan spectra of the as-synthesized  $\text{MgMoO}_4$  sample (Fig. S3) displays the main elements (Mg 2p, Mo 3d, O 1s and C 1s). The ratios of Mo:O were in good agreement with is expected for molybdates (1:4). The atomic percentages of the elements calculated from the wide spectrum are found to be Mg (13.3%); Mo (13.3%), O (52.0), C (20.7%) and S (0.7%). The narrow scan spectra for the elements Mg 1s, Mo 3d, C 1s and O 1s are shown in Figs. 5a-e. The Mg 1s and *KLL* peak (Fig. 5a) are centred at 1303.8 eV (binding energy) and 1181.8 eV (kinetic energy) respectively, which is in good agreement with the reported value in the XPS database.<sup>18</sup> The doublet at 231 eV and 234.1 eV in Fig. 5b are attributed to  $\text{Mo}3d_{5/2}$  and  $\text{Mo}3d_{3/2}$ , respectively.<sup>19</sup> The Mo 3d region was fitted with two doublets, one doublet with an asymmetric LF(1.3,5,55,300) line shape for  $\text{Mo}^{6+}$  and one doublet with a symmetric GL(30) at lower binding energy resulting due to X-ray induced reduction of the Mo. While the Mo 3p (in Fig. 5c) obscures the presence of an N 1s peak but a possible fit to this region is presented and the remaining area is then fitted with a single N 1s peak centred at 400 eV attributed to C-NH<sub>2</sub> from urea as a fuel. C 1s spectra (Fig. 5d) were fitted with three components at 284.6 – 285 eV, 286.3 – 286. 7 eV, and 288.6 eV and assigned to C- C, C- O, and C=O respectively. The former component could be likely due to adventitious hydrocarbon contamination while the other two may be attributed to residual urea from the synthesis. The O 1s components (Fig. 5e) were fitted to two components, one calibrated for the metal oxide at 530. 45 eV and the other one for carbon-oxygen species, around 532 eV. The results for the XPS is consistent with the XRD results and indicate that the phase pure material is also found at the surface and has been obtained through combustion synthesis

### ***Electrochemical characterization of platelike $\text{MgMoO}_4$ crystallites for capacitor applications***

The hybrid capacitor, coupling magnesium molybdate ( $\text{MgMoO}_4$ ) with activated carbon, is a potential candidate to enhance the electrochemical properties of capacitors. To evaluate this

electrochemically and to understand the unrevealed redox mechanism, initially, the  $\text{MgMoO}_4$  was tested as a single electrode and then fabricated as a device to examine its suitability for energy storage devices. To understand the effect of replacing aqueous 2M NaOH with non-aqueous 1M  $\text{NaClO}_4$  in EC: DMC: FEC in  $\text{MgMoO}_4$ | AC cell, we have carried out experiments in aqueous and non-aqueous electrolytes. The specific capacitance of each electrode of the hybrid cell was evaluated by potentiostatic and galvanostatic mode and the profiles are shown in Figs. 6-7.

### *Aqueous Electrolyte*

#### *(a) Single cell characteristics – $\text{MgMoO}_4$ and activated carbon*

Figure 6a shows the comparison of cyclic voltammetry (CV) curves using the  $\text{MgMoO}_4$  as an electrode in a three-electrode configuration at different sweep rates in 2 M NaOH aqueous electrolyte. The electrode was measured with a potential window of 0.6 V and all the curves exhibit a quasi-rectangular shape, indicating typical characteristics of asymmetric capacitive behaviour. No clear peaks corresponding to oxidation or reduction are seen in the CV profile. The calculated specific capacitances from the cyclic voltammetry are 207, 188, 177, and 150 F/g at a sweep rate of 1, 2, 3 and 5 mV/s, respectively. The capacitance values were determined by integrating the area under the CV curve as a function of sweep rate. The observed trend indicates a diffusion-controlled redox reaction. The electrochemical behaviour of  $\text{MgMoO}_4$  in aqueous NaOH is associated with the electron-transfer mechanism involving the ability of  $\text{OH}^-$  to be adsorbed and desorbed reversibly. They also may be reversibly intercalated into the oxidised form of  $\text{Mg}(\text{OH})_2$  reversibly for the faradaic process forming  $\text{MgOOH}$ , which could be attributed to the pseudo-capacitance. Since Mg is an alkaline earth metal, which exhibits oxidation states of zero (metal) and two (in all Mg compounds), the redox reactions of binary metal oxide like  $\text{MgMoO}_4$  can be attributed to the other Mo cation, since Mo possesses multiple oxidation states. However, it has been reported<sup>19</sup> that in alkaline

solutions i.e. NaOH of around pH 9, the molybdate species exist only as  $\text{MoO}_4$ . However, in the presence of excess  $\text{OH}^-$  ions it forms as  $\text{Mo}(\text{OH})_3$  prior to any electrochemical measurements.  $\text{Mo}(\text{OH})_3$  does not exhibit any redox peaks in the pH range 7 – 12<sup>20</sup>, so the only plausible mechanism could be  $\text{OH}^-$  ions forming a double layer on the surface of  $\text{Mg}(\text{OH})_2$  and intercalating into Mg sites forming  $\text{MgOOH}$ . Based on this, we can see the curves are reversible and stable within the given potential window contributing to 200 F/g specific capacitance. The charge – discharge behaviour for the  $\text{MgMoO}_4$  was investigated at four different current densities with an identical voltage window of 0.6 V. Typical voltage profiles are shown in Fig. 6b. The material showed a near-symmetric behaviour upon reversing the polarity, indicating a good reversibility. A triangular shape without any significant ohmic drop or plateau like a curve, indicate good charge transport and a material which is capacitive in nature. The calculated discharge capacitances for the charge-discharge curves are very similar to those obtained from the CV curves, with a high capacitance of 200 F/g at 0.5 A/g. Therefore,  $\text{MgMoO}_4$  is a good candidate for a positive electrode. Conventional activated carbon (AC) has been used for negative electrodes; the typical curve for single electrode AC and  $\text{MgMoO}_4$  are compared in Fig. 6c. The shape of the CV curve for the AC electrode in the negative potential range of -1.0 V exhibits a nearly ideal rectangular shape, which is a clear representation of electrochemical double layer (EDL) capacitor behaviour.<sup>6</sup> A value of 125 F/g was calculated for the negative electrode of activated carbon, derived from the non-faradaic mechanism. The behaviour and potential range of AC differs from that of  $\text{MgMoO}_4$  as shown in Fig. 6c. The AC is capacitive in nature while the  $\text{MgMoO}_4$  behaves like a pseudocapacitive type material.<sup>6-7</sup> Overall, the operating voltage for this hybrid cell could be 1.6 V. Although the area of the CV curve for AC is larger than that of the  $\text{MgMoO}_4$  the oxide has an extended voltage window than the positive electrode. In order to

ensure the charge balance of the hybrid cell, the weight ratio between the negative and positive electrodes was 1:0.375 (Eq. 3).

*(b) Hybrid cell characteristics – MgMoO<sub>4</sub> vs. activated carbon*

The typical CV of a hybrid cell is shown in Fig. 6d. The hybrid cell was cycled between 0 and 1.6 V at various current densities and exhibited an excellent reversibility. The observed integral part of the curve increases when increasing the scan rate, attributed to increased mass rate. At a higher scan rate (5 mV/s), the anodic peak potential shifted in the positive direction (+0.4 V; as indicated in the Fig. 6d) suggesting higher potentials are needed for the same product to occur. Notably, the separation between the oxidation and reduction peaks during the forward and reverse scans widens, the more irreversible is the electrode process at a very high scan rates.<sup>21</sup> Among the performed CV profiles at various current densities, higher sweep rates (3 mV/s and 5 mV/s) show a clear Faradaic current but have a broad reduction peak. The calculated specific capacitances from the cyclic voltammetry are 52, 43, 34, and 25 F/g at a sweep rate of 1, 2, 3 and 5 mV/s, respectively. Clearly, a pair of peaks is observed during the oxidation and subsequent reduction, indicating that the electrochemical processes include both faradaic (pseudocapacitance) and non-faradaic (double layer capacitance) mechanisms, thereby it is a pseudocapacitive material. Testing in galvanic mode resulted in very similar behaviour, with distorted triangular-shaped charge-discharge curves resulting (Fig. 6e). Undoubtedly, this excellent performance in stems from the hierarchical plate-like structure of the material. The Nyquist plot of the single and hybrid cell has been compared in Fig. 6f. In the high frequency region, the internal resistance is quite low for both the cells and hence the observed low IR drop in the galvanostatic plots (Fig. 6b, 6e) and there is not much difference seen in charge transfer resistance (Fig. 6e). However, in the low frequency region, the vertical line indicates a capacitive behaviour, which is more pronounced for the single cell than the hybrid.

### *Non- aqueous Electrolyte*

Figure 7a shows comparative cyclic voltammetric curves for MgMoO<sub>4</sub> and AC in the non-aqueous electrolyte, tested in the two-electrode configuration using metallic sodium as an anode. The specific capacitance for the MgMoO<sub>4</sub> and AC measured in the two-electrode system within the potential window of 2.0 V was calculated to be 64 F/g and 20 F/g, respectively. Interestingly, a reversible capacitance of ~ 60 F/g is observed for MgMoO<sub>4</sub> in the half-cell (two-electrode) configuration, which is about three times lower than that observed for the aqueous electrolyte. The CV curve of MgMoO<sub>4</sub> exhibits a well-defined reduction (C<sub>1</sub> = 0.58 V) and oxidation peak (A<sub>1</sub> = 0.85 V), corresponding to the faradaic redox reactions,  $\text{Mo}^{6+} \leftrightarrow \text{Mo}^{4+} + 2\text{e}^-$ , which is a characteristic of pseudocapacitive behaviour.<sup>6</sup> The CV shape of the AC in the potential range of 2 V is quite different to that of the MgMoO<sub>4</sub> pseudocapacitive behaviour because the overall capacitance of the AC arise solely from the EDL.<sup>6</sup> A near- rectangular shape with no obvious redox peaks is an indication of EDL behavior. The charge balance of the hybrid cell between the negative and positive electrodes was 1:3.2. Therefore, the sodium ion capacitor using a non-aqueous solution comprises of an intercalation anode and a surface adsorption cathode where Na<sup>+</sup> and ClO<sub>4</sub><sup>-</sup> counter ions acts as charge carriers. The typical CV curve of the hybrid cell is shown in Fig. 7b. A quasi-rectangular shaped CV with peak-like shoulder is visible, indicating that the carbon electrode will reversibly adsorb ClO<sub>4</sub><sup>-</sup> and release Na<sup>+</sup> while MgMoO<sub>4</sub> involves pseudocapacitive redox interaction of Mo<sup>6+</sup> ions. The resulting capacitance of 34 F/g is therefore achieved both by EDL and pseudocapacitance.

With increasing scan rate to 6 mV/s, the cell displayed negligible shape distortion of the original CV, which shows that the material is desirable for fast discharge / charge in power applications. Figs. 7c-e shows the galvanostatic charge/discharge profiles for various current rates as well as cycling stability at 2 A/g. The specific capacitances of the hybrid cell are 38,



35, 32, and 30 F/g at 1.2, 1.4, 1.6 and 2 A/g, respectively. This suggests that the electrodes are sustainable at a higher current rate, however, the curves are asymmetrical with high IR drops. The shape of the charge-discharge curves for the consecutive cycles are also shown in Fig. 7d. Conversely, at a lower current rate of 0.2 A/g the curves (in Fig. 7e) are symmetrical with a low IR drop, an improved capacitance of 45 F/g and showing excellent reversibility for multiple cycles. The Nyquist plots of the half-cell configuration and hybrid cell are compared in Fig. 7f. In the high frequency region between 0 and 200  $Z'\Omega^{-1}$  a clear semicircle is observed followed by a weakly rising trend in the intermediate to low frequency region. Compared to the hybrid cell, a smaller semicircle is observed for half-cell (single) configuration indicating low interfacial charge-transfer resistance.<sup>22</sup> Thereafter, the trend rises almost vertically, which is indicative of the good capacitive performance of the fabricated device. Therefore, the superior electrochemical performance with excellent storage retention and reversibility of the aqueous electrolyte can be attributed to the higher ionic conductivity and fast electron kinetics.<sup>23</sup>

The primary objective of the current work is to enhance the energy and power densities of the supercapacitor. To demonstrate the operational characteristics of the two systems evaluated here, the energy density, the Ragone plot, and cycling stability are shown in Fig. 8. The energy density plots of the hybrid cell at various current densities are shown in Fig. 8a. A high energy density value (250 Wh/kg at 0.2 A/g) obtained for the non-aqueous system has been significantly greater than those reported for the hybrid sodium-ion capacitors tested in organic  $\text{NaClO}_4$  electrolyte.<sup>15, 24</sup> Even when tested at a higher value of current density (2 A/g), the energy density is retained to 135 Wh/kg. In the case of an aqueous system tested here, the energy density of 60 Wh/kg was four times lower than the non-aqueous counterpart. Nevertheless, the retention rate was higher than the non-aqueous system and comparable to those of the values reported in the literature for cobalt and nickel

molybdates tested in aqueous electrolytes.<sup>25-26</sup> The lower value of energy density in aqueous systems results from the 2 V cell limit to avoid the decomposition of water. The Ragone plot of the hybrid cell (Fig. 8b) in non-aqueous electrolyte shows a high energy density of 250 Wh/kg is achieved at a power density 1500 W/Kg. Even at a high power density of 9720 W/kg, the device still has an energy density of 135 Wh/kg. This performance is superior to that of aqueous supercapacitors tested here (5760 W/kg at 32 Wh/kg) and to that of several hybrid materials, including hierarchical structures, reported in the literature.<sup>27-30</sup> These results demonstrate the importance and great potential application of MgMoO<sub>4</sub> platelike architectures<sup>31</sup> in the development of energy storage systems. The cycling stability of the hybrid cell (Fig. 8c) is further evaluated at a constant current density of 1 A/g for 1000 cycles and obviously the aqueous system shows much improved performance with higher capacitance retention as compared to the non-aqueous system. The differences in the mechanisms through which MgMoO<sub>4</sub> undergoes electrochemical processes in aqueous NaOH and non-aqueous NaClO<sub>4</sub> can occur be explained in terms of the formation of product such as MgOOH through OH<sup>-</sup> ions ad- and desorption properties. This may be attributed to the higher ionic conductivity and faster alkali ion transport in aqueous systems. The results in both electrolytes are encouraging but the cycling stability and capacitance retention need to be significantly improved for the non-aqueous system to be suitable for practical power devices.

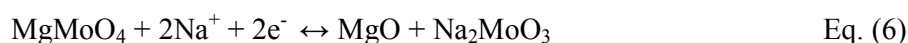
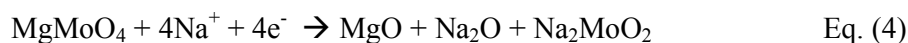
#### ***Electrochemical characterization of platelike MgMoO<sub>4</sub> crystallites for battery applications***

MgMoO<sub>4</sub> were also tested as an anode for sodium ion battery. The CV profile of the MgMoO<sub>4</sub> was recorded in the voltage of 0.005 – 2.5 V vs. Na at a sweep rate of 2 mV/s (Fig. 9a). The characteristics of the first cycle are quite different to those of the subsequent cycles. The first sweep was initiated in the cathodic direction and then reversed back anodically to 2.5 V. While two peaks C<sub>1</sub> and C<sub>2</sub> at 1.1 and 0.45 V are visible in the first reduction, one

broad peak at  $A_1$  at 0.9 is observed in the subsequent oxidation. In the subsequent cycles, the cathodic peaks  $C_1$  and  $C_2$  shifted to lower potentials to 0.68 and 0.21 with reduced peak currents while the anodic peak  $A_1$  remained unchanged. The cathodic reduction of  $MgMoO_4$  gave rise to three distinct materials as shown in Eq. 4, such as  $MgO$ ,  $Na_2MoO_2$ ,  $Na_2O$  and oxidation of these materials resulted in the original  $MgMoO_4$  material (Eq. 5). The second reduction profile showed that these peaks shifted to lower potentials corresponding to the formation of  $MgO$  and  $Na_2MoO_3$  (Eq. 6) which is reversible and the subsequent profiles are qualitatively similar. Overall, the shape of the subsequent discharge and charge curves are almost identical in the second and fifth cycles, though the discharge curves are not exactly superimposable as charge process. This minor discrepancy could be attributed to the stabilization process of the electrode that depends on the quality of the solid electrolyte interphase (SEI) layer formed on the surface.<sup>32</sup> The electrochemistry of the redox mechanism and the formation of materials formed in sodium-ion batteries for molybdates are not well proposed in the literature yet.

The storage and cycling properties of  $MgMoO_4$  were investigated by galvanostatic cycling with the voltage window 0.005 – 2.5 V vs. Na at a current of  $C/10$  rate and the profiles are shown in Fig. 9b. The shape of the first discharge profile (labelled 1) is characterized by an initial drop in voltage (from open-circuit voltage OCV 2.4 V) to 1.0 V, followed by a long plateau at 0.8 V and then a long downward sloping potential profile until the cut off voltage. The  $MgMoO_4$  electrode produced a first discharge capacity of 580 mAh/g as a cathode material in a sodium-ion battery, corresponding to the insertion of 4  $Na^+$  equivalents per mole of  $MgMoO_4$  (1 mol. of Na corresponds to the capacity of 145 mAh/g). Upon charging (up to 2.5 V), the cell voltage climbed roughly linearly with time to 1.2 V and a gradual rise to 2.5 V is seen. The initial discharge and charge capacities are 590 mAh/g and 292 mAh/g, respectively. The observed irreversible capacity is due to the formation of a

passivation layer, called solid electrolyte interphase (SEI), on the surface of MgMoO<sub>4</sub> electrode during the initial cycles.<sup>33</sup> This layer protects the electrolyte from further loss of capacity in the successive cycles. The discharge profile in Fig. 9b has been divided into regions marked with “A” and “B” and we proposed a reaction mechanism, involving the formation of various compounds during the redox reactions. The amorphization of the MgMoO<sub>4</sub> and a long plateau at 0.8 V in the region A, consume 2 mol of Na (about 292 mAh/g after subtracting the C and binder – content), which is reversible. At the location B, MgMoO<sub>4</sub> has converted to irreversible Na<sub>2</sub>O consuming another 2 mol. of Na, totalling 590 mAh/g, as per Eq. 4.



The charge curve corresponds to the formation of products shown in Eq. 5, which reforms the starting material. The subsequent discharge-charge curves correspond to Eq. 6, which is equivalent to 2 mol of Na insertion of reversible capacity 292 mAh/g. The Mg<sup>2+</sup> ion in MgMoO<sub>4</sub> is not expected to be reduced to Mg metal under room-temperature electrochemical conditions. The charge and discharge capacities of the MgMoO<sub>4</sub> (Fig. 9b) were stable at approximately 250 mAh/g and no significant capacity loss was observed for the first 75 cycles. The rate capability of the electrode was cycle tested at various current densities ranging from 0.04 to 0.32 A/g and the plots are shown in Fig. 9c. When the current density was increased stepwise from 0.04 to 0.08, 0.16 and 0.32 A/g and tested for ten cycles, the average discharge capacity was found to be 210, 135, 90, 70 mAh/g, respectively. Upon reverting the current density back to 0.04 A/g, an average discharge capacity as high as 175 mAh/g could be recovered. Based on these results, we suggest that the MgMoO<sub>4</sub> nanoplates

with hierarchical architecture are strong anode candidates among the available conventional hard carbon materials<sup>34</sup> of sodium-ion battery because of the excellent cyclability, reversibility and rate capability.

### **Conclusions**

MgMoO<sub>4</sub> was successfully synthesized by the combustion route. Microscopy confirmed the morphology was plate-like and structure was hierarchical in nature. X-ray diffraction and X-ray photoelectron spectroscopy confirmed that despite the low temperature route used for synthesis, the MgMoO<sub>4</sub> phase was obtained with good crystallinity and with all elements in their expected valence states. The highly porous, high surface area phase makes it a potential candidate for energy storage devices like supercapacitors and rechargeable battery in sodium based systems. Fast charge storage and cycling properties of MgMoO<sub>4</sub> electrodes were examined against conventional activated carbon and in a hybrid device. The effect of electrolyte, both aqueous and non-aqueous, was also investigated. The assembled hybrid cell in an aqueous electrolyte exhibited a specific capacitance of 43 F/g at 2 A/g, whereas, in the non-aqueous system for the same current density the available capacitance reduced to 30 F/g. This could be attributed to the highly conducting aqueous electrolyte enabling conductive paths for electron transfer and efficient ion access, thus the improved performance. The capacitance retention was found to be higher (over 95% after 1000 cycles) in aqueous electrolytes. Notably, the aqueous cell was limited by the 2 V voltage window and hence produced lower energy and power density. The high power performance of the non-aqueous system suggests that there is potential as an electrode for the sodium-ion capacitor. When MgMoO<sub>4</sub> was used as anode material for sodium-ion battery, it delivered a specific discharge capacity of 590 mAh/g. This is equivalent to 4 mol of Na insertion only 2 mol of which is reversible. The battery showed excellent cycling stability with no significant loss in

capacity and exhibited high rate capability. After 75 cycles, the  $\text{MgMoO}_4$  electrode retained 225 mAh/g. The charge-discharge mechanisms are proposed for sodium ion battery.

### Acknowledgement

Karlsruhe Institute of Technology (KIT) is acknowledged for providing a visiting fellowship and to accommodate (M. M) at HIU and carry out the electrochemical work. The STEM work was carried out using a JEOL ARM200F instrument equipment funded by the Australian Research Council (ARC) – Linkage, Infrastructure, Equipment and Facilities (LIEF) grant LE120100104, located at the UOW Electron Microscopy Centre. This work was performed in part at the Australian National Fabrication Facility (ANFF), a company established under the National Collaborative Research Infrastructure Strategy, through the La Trobe University Centre for Materials and Surface Science.

### References

1. Z. Lei, J. Zhang, L. L. Zhang, N. A. Kumar and X. S. Zhao, Functionalization of chemically derived graphene for improving its electrocapacitive energy storage properties. *Energy Environ. Sci.* **2016**, 9, 1891 - 1930.
2. N. Armaroli and V. Balzani, The future of energy supply: challenges and opportunities. *Angew. Chem. Int. Ed.*, **2007**, 45, 52-56.
3. B. Li, M. Zheng, H. Xue and H. Pang, High performance electrochemical capacitor materials focusing on nickel based materials. *Inorg. Chem. Front.* **2016**, 3, 175 - 202.
4. Y. Wang, Y. Song and Y. Xia, Electrochemical capacitors: mechanism, materials, systems, characterization and applications. *Chem. Soc. Rev.* **2016**, 45, 5925 - 5950.
5. W. Zuo, R. Li, C. Zhou, Y. Li, J. Xia, and J. Liu, Battery-Supercapacitor hybrid devices: Recent progress and future prospects. *Adv. Sci.* 2017, 4, 1600539.
6. D. P. Dubal, O. Ayyad, V. Ruiz, and P. Gomez- Romero, Hybrid energy storage: the merging of battery and supercapacitor chemistries. *Chem. Soc. Rev.* **2015**, 44, 1777 - 1790.
7. Y. Han, Z. Lai, Z. Wang, M. Yu, Y. Tong, and X. Lu, Designing carbon based supercapacitors with high energy density: A minireview of recent progresses. *Chem. Eur. J.* 10.1002/chem.201705555.
8. Z. Zhang, Y. Liu, Z. Huang, L. Ren, X. Qi, X. Wei and J. Zhong, Facile hydrothermal synthesis of  $\text{NiMoO}_4@\text{CoMoO}_4$  hierarchical nanospheres for supercapacitor applications. *Phys. Chem. Chem. Phys.* **2015**, 17, 20795-20804.
9. J. Candler, T. Elmore, B. K. Gupta, L. Dong, S. Palchoudhury and R. K. Gupta, New insight into high-temperature driven morphology reliant  $\text{CoMoO}_4$  flexible supercapacitors. *New J. Chem.* **2015**, 39, 6108-6116.

10. B. Senthilkumar, R. Kalai Selvan, D. Meyrick and M. Minakshi, Synthesis and characterization of manganese molybdate for symmetric capacitor applications, *Int. J. Electrochem. Sci.*, **2015**, 10, 185 - 193.
11. M. J. Barmi and M. Minakshi, Role of polymeric surfactant in the synthesis of cobalt molybdate nanospheres for hybrid capacitor applications. *RSC Adv.* **2016**, 6, 36152-36162.
12. P. R. Jothi, K. Shanthi, R. R. Salunkhe, M. Pramanik, V. Malgras, S. A. Alshehri and Y. Yamauchi, Synthesis and Characterisation of  $\alpha$ -NiMnO<sub>4</sub> nanorods for supercapacitor application. *Eur. J. Inorg. Chem.* **2015**, 3694-3699.
13. T. Watcharatharapong, M. Minakshi Sundaram, S. Chakraborty, D. Li, GM. Shafiullah, R.D. Aughterson and R. Ahuja, Effect of transition metal cations on stability enhancement for molybdate-based hybrid supercapacitor, *ACS Applied Mater. Interface* **2017**, 9, 17977 - 17991.
14. G. Aranovich and M. Donohue, Analysis of Adsorption Isotherms: Lattice theory predictions, classifications of isotherms for gas-solid equilibria, and similarities in gas and liquid adsorption behaviour, *J. Colloids and Inter. Sci.* **1998**, 200, 273 – 290.
15. Z. Chen, V. Augustyn, X. Jia, Q. Xiao, B. Dunn, and Y. Lu, High-performance sodium-ion pseudocapacitors based on hierarchically porous nanowire composites, *ACS Nano*, **2012**, 6, 4319 – 4327.
16. G. Zhang, H. Wang, S. Zhang, and C. Deng, Using core-shell interlinked polymer@C-iodine hollow spheres to synergistically depress polyiodide shuttle and boost kinetics for iodine-based batteries, *J. Mater. Chem. A.* **2018**, 6, 9019 – 9031.
17. L. Ke, J. Dong, B. Lin, T. Yu, H. Wang, S. Zhang, and C. Deng, A NaV<sub>3</sub>(PO<sub>4</sub>)<sub>3</sub>@C hierarchical nanofiber in high alignment: exploring a novel high-performance anode for aqueous rechargeable sodium batteries, *Nanoscale* **2017**, 9, 4183 – 4190.
18. A. V. Naumkin, A. Kraut-Vass, S. W. Gaarenstroom C. J., Powell, NIST X-ray Photoelectron Spectroscopy Database v4.1. **2012**; <http://srdata.nist.gov/xps/>.
19. J. Baltrusaitis, B. M.-Sanchez, V. Fernandez, R. Veenstra, N. Dukstiene, A. Roberts, and N. Fairley, Generalized molybdenum oxide surface chemical state XPS determination via informed amorphous sample model, *App. Surf. Sci.* **2015**, 326, 151 – 161.
20. C. V. Krishnan, M. Garnett, B. Hsiao, and B. Chu, Electrochemical measurements of isopolyoxomolybdates: 1. pH dependent behaviour of sodium molybdate, *Int. J. Electrochem. Soc.* **2007**, 2, 29 – 51.
21. D. Tu, B. Wu, B. Wang, C. Deng, and Y. Gao, A highly active carbon-supported PdSn catalyst for formic acid electrooxidation, *Appl. Catalysis B: Environmental* **2011**, 103, 163 – 168.
22. C. Deng, S. Zhang, H. Wang, and G. Zhang, “Bubble-in-nanorod” hierarchical hybrid fibre: A highly efficient design for pyrophosphate-based freestanding cathodes towards fast sodium/lithium intercalation” *Nano Energy* **2018**, 49, 419 – 433.
23. W. Wu, S. Shenbag, J. Chang, A. Rutt, and J. F. Whitacre, Relating electrolytic concentration to performance and stability for NaTi<sub>2</sub>(PO<sub>4</sub>)<sub>3</sub>/Na<sub>0.44</sub>MnO<sub>2</sub> Aqueous sodium-ion batteries, *J. Electrochem. Soc.* **2015**, 162(6), A803-A808.
24. J. Yin, L. Qi, and H. Wang, Sodium titanate nanotubes as negative electrode materials for sodium-ion capacitors, *ACS App. Mater. Inter.* **2012**, 4, 2762 – 2768.
25. S. Peng, L. Li, H. B. Wu, S. Madhavi, and X. W. Lou, Controlled growth of NiMoO<sub>4</sub> nanosheet and nanorod arrays on various conductive substrates as advanced electrodes for asymmetric supercapacitors, *Adv. Energy. Mater.* **2015**, 5, 1401172.
26. G. K. Veerasubramani, K. Krishnamoorthy, S. Radhakrishnan, N.-J. Kim, and S. J. Kim, Synthesis, characterization, and electrochemical properties of CoMoO<sub>4</sub> nanostructures, *Int. J. Hyd. Energy*, **2014**, 39, 5186–5193.

27. Y. Zeng, X. Zhang, Y. Meng, M. Yu, J. Yi, Y. Wu, X. Lu, and Y. Tong, Achieving ultrahigh energy density and long durability in a flexible rechargeable quasi-solid-state Zn-MnO<sub>2</sub> battery, *Adv. Mater.* **2017**, 29, 1700274.
28. Q.T. Qu, Y. Shi, S. Tian, Y. H. Chen, Y. P. Wu, and R. Holze, A new cheap asymmetric aqueous supercapacitor: activated carbon//MnO<sub>2</sub>, *J. Power Sour.* **2009**, 194, 1222 – 1225.
29. X. Liu, N. Zhang, J. Ni, and L. Gao, Improved electrochemical performance of sol-gel method prepared Na<sub>4</sub>Mn<sub>9</sub>O<sub>18</sub> in aqueous hybrid Na-ion supercapacitor, *J. Solid State Electrochem.* **2013**, 17, 1939 – 1944.
30. C. Tang, Z. Tang, and H. Gong, Hierarchically porous Ni-Co oxide for high reversibility asymmetric full-cell supercapacitors, *J. Electrochem. Soc.* **2012**, 159, A651 – A656.
31. L. Zhang, W. He, M. Ling, K. Shen, Y. Liu, and S. Guo, Self-standing MgMoO<sub>4</sub>/Reduced graphene oxide nanosheet arrays for lithium and sodium ion storage, *Electrochim. Acta.* **2017**, 252, 322 – 330.
32. L. Zhang, W. He, M. Ling, K. Shen, Y. Liu, and S. Guo, Controllable synthesis of hierarchical MgMoO<sub>4</sub> nanosheet-arrays and nano-flowers assembled with mesoporous ultrathin nanosheets, *J. Phys. Chem. Solids*, **2018**, 115, 215 – 220.
33. L.-Y. Kuo, A. Moradabadi, H.-F. Huang, B. J. Hwang, and P. Kaghazchi, Structure and ionic conductivity of the solid electrolyte interphase layer on tin anodes in Na-ion batteries, *J. Power Sour.* **2017**, 341, 107 – 113.
34. H. Hou, X. Qiu, W. Wei, Y. Zhang, and X. Ji, Carbon anode materials for advanced sodium-ion batteries, *Adv. Energy Mater.* **2017**, 7, 1602898.



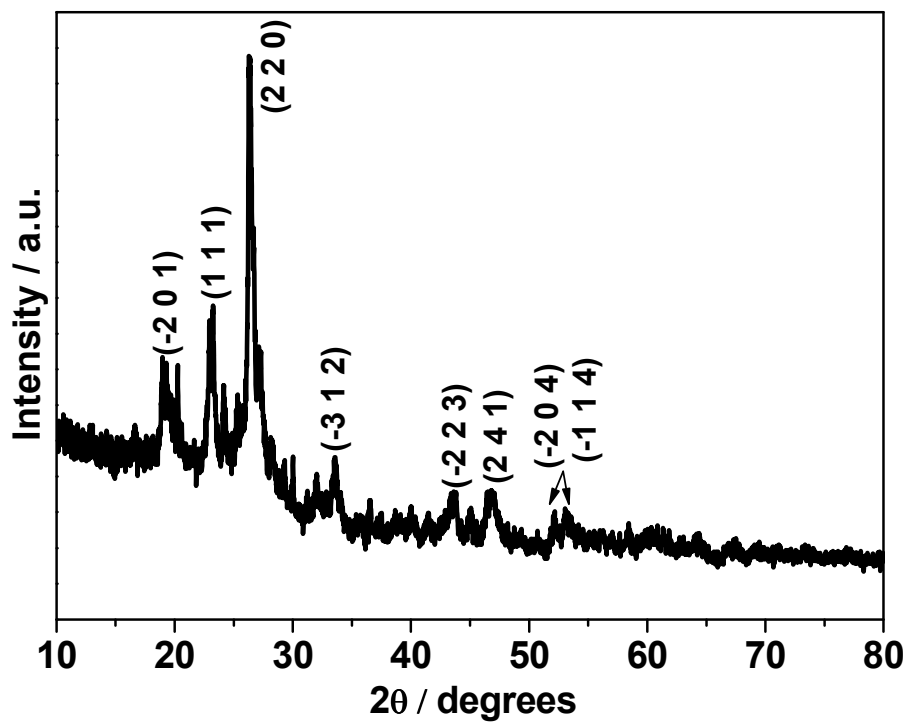
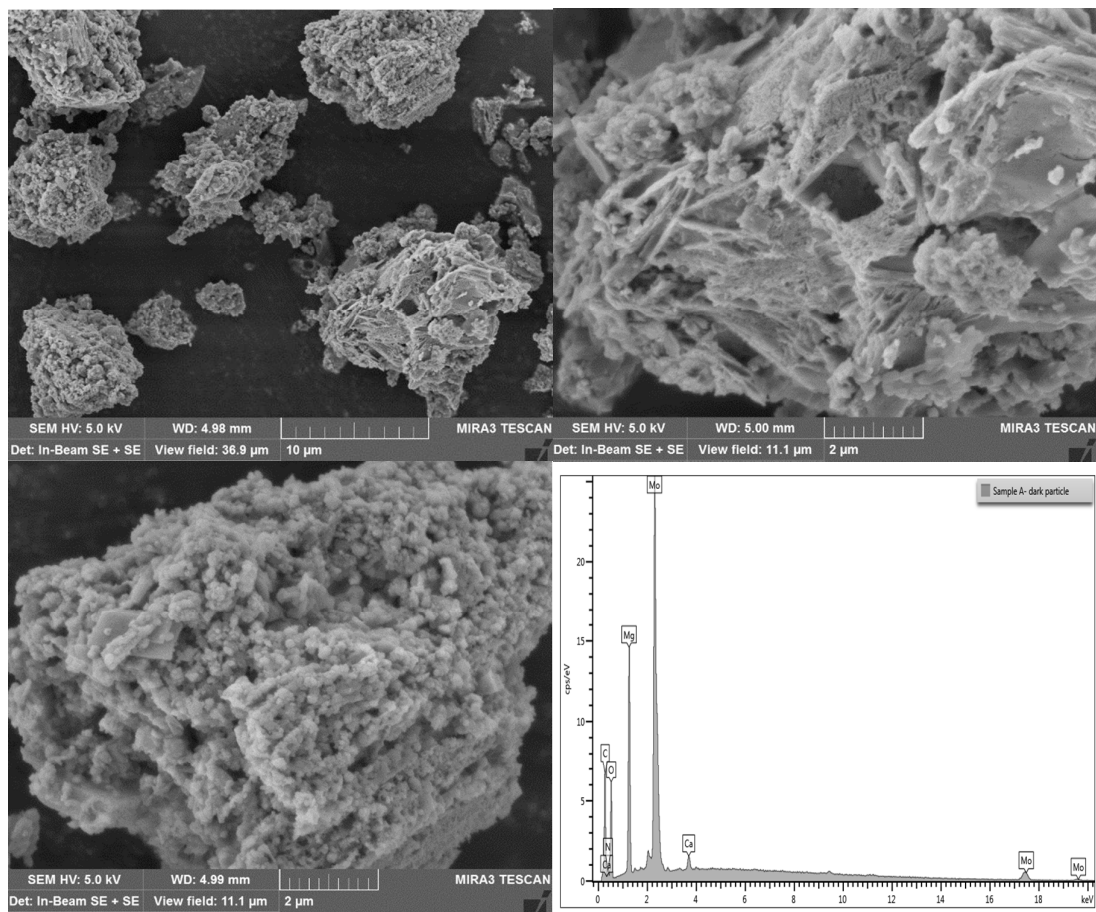
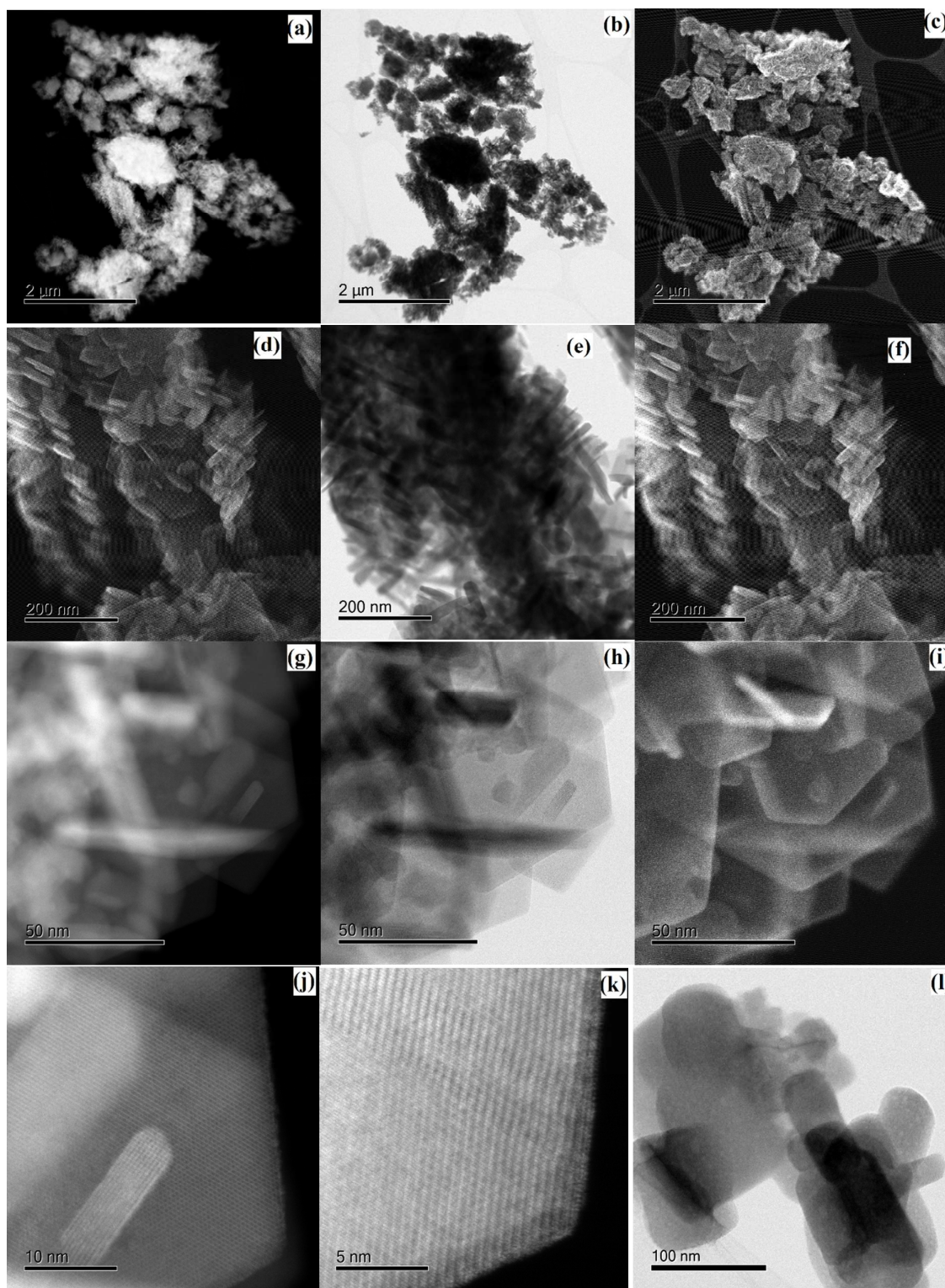


Figure 1 X-ray diffraction (XRD) pattern of MgMoO<sub>4</sub> nanoplates.



**Figure 2** (a) Low and (b-c) high magnifications SEM images of MgMoO<sub>4</sub> illustrating the formation of numerous plate shaped particles with a porous structure in different locations. (d) EDS analysis showing the elemental composition of Mg, Mo, C and O.



**Figure 3** (a, d, g, j and k) HAADF STEM images, (b, e, h and l) BF images, and (c, f and i) SE images of  $\text{MgMoO}_4$ . (a-c) Low magnification images, (d-f) plate-shaped twinned particles. (g-i) Typical  $\text{MgMoO}_4$  showing nanoplate hierarchical architecture. (j) thin overlapping plates, (k) high magnification of plate showing high degree of crystallinity with weak mottling due to fine scale porosity (l) 5-25nm pores in  $\text{MgMoO}_4$  plates.

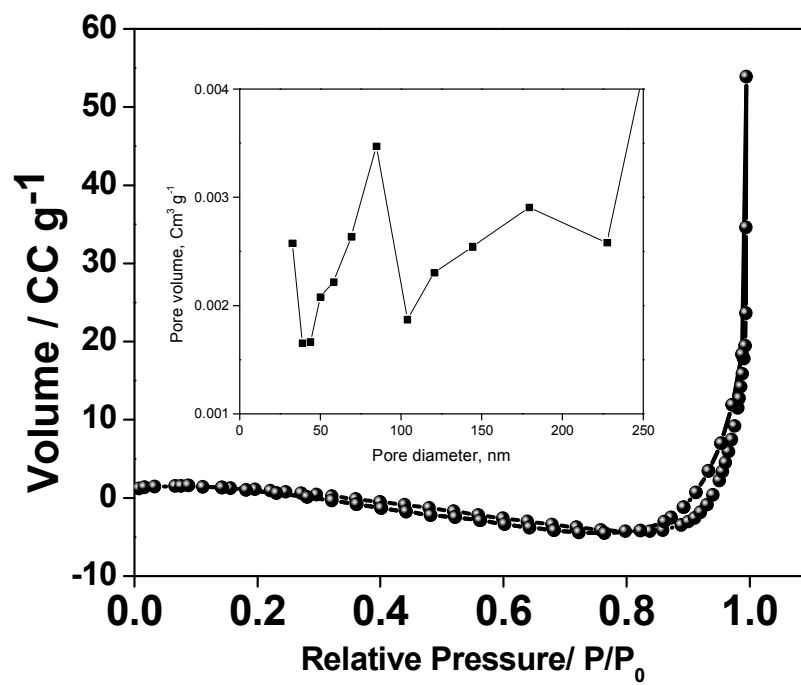


**Figure 4** Nitrogen adsorption and desorption isotherm and inset showing BJH adsorption pore size distribution of MgMoO<sub>4</sub>.

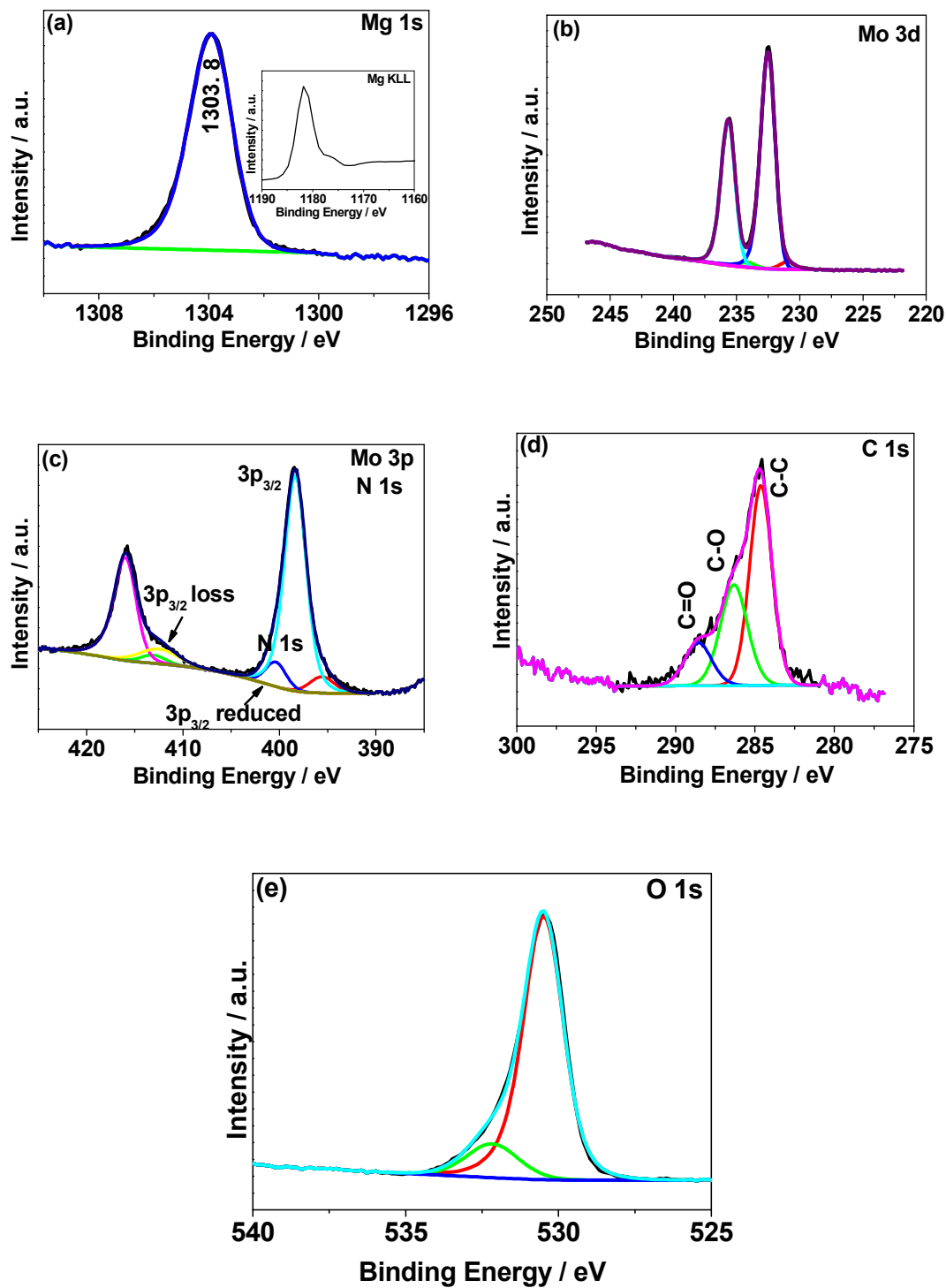


**Figure 5** X-ray photoelectron spectroscopy (XPS) spectra of MgMoO<sub>4</sub>. High resolution spectra for regions (a) Mg 1s, (b) Mo 3d, (c) Mo 3p, (d) C 1s, and (e) O 1s.

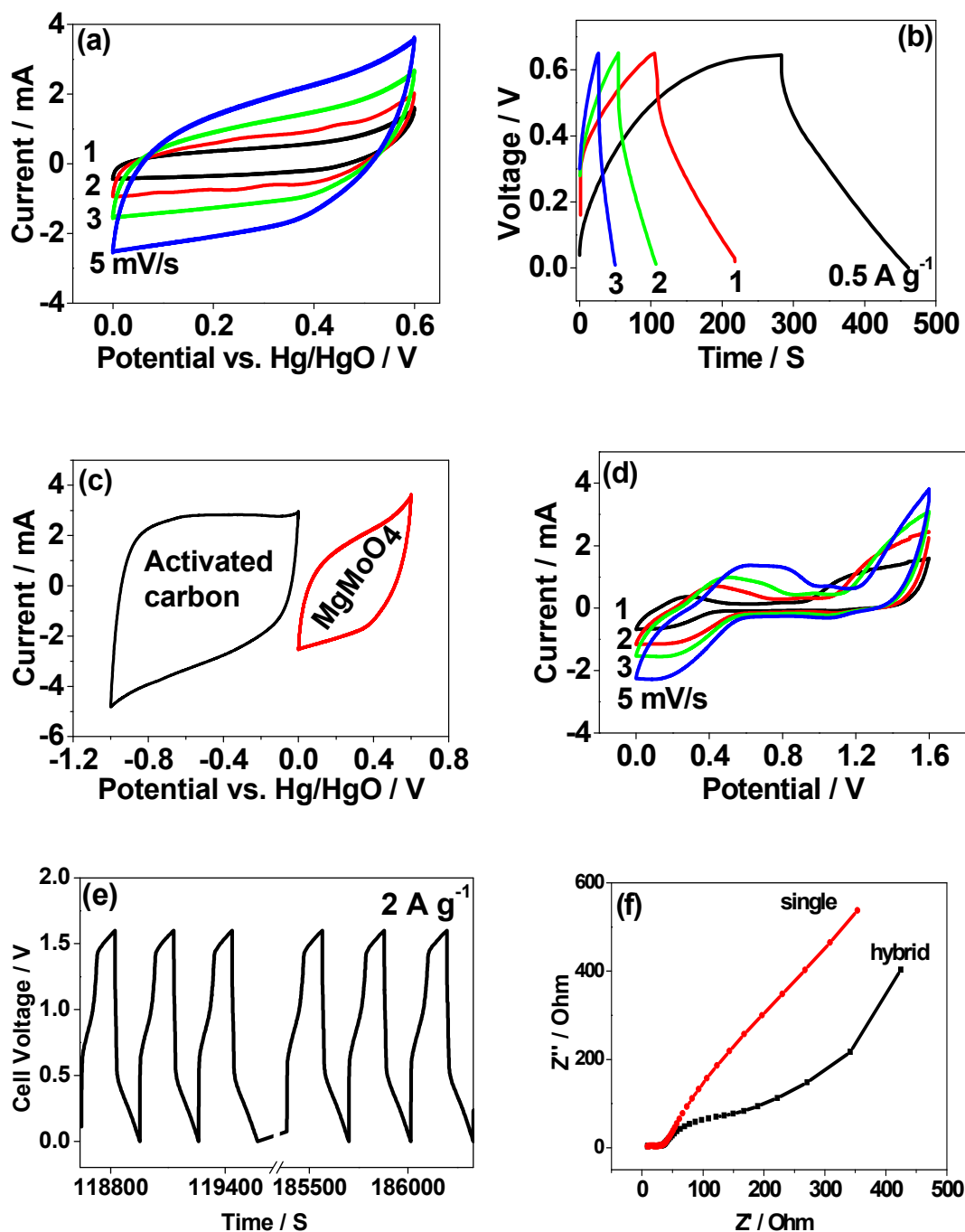


**Figure 6** (a) First cyclic voltammetric (CV) curves, and (b) charge-discharge behaviour (three-electrode configuration) of MgMoO<sub>4</sub> electrode. (c) CV curves (three-electrode configuration) of MgMoO<sub>4</sub> as positive compared with activated carbon as negative electrode. Hybrid cell (two-electrode configuration) (d) CV and (e) charge-discharge curves of supercapacitors comprising AC || MgMoO<sub>4</sub> in 2M NaOH aqueous electrolyte. Both CV and charge-discharge curves show pseudocapacitive behaviour, (f) Nyquist plot comparing the impedance in high frequency region and capacitive behaviour in low frequency region for single and hybrid cell. Sweep rates and current density are indicated in the respective figures.

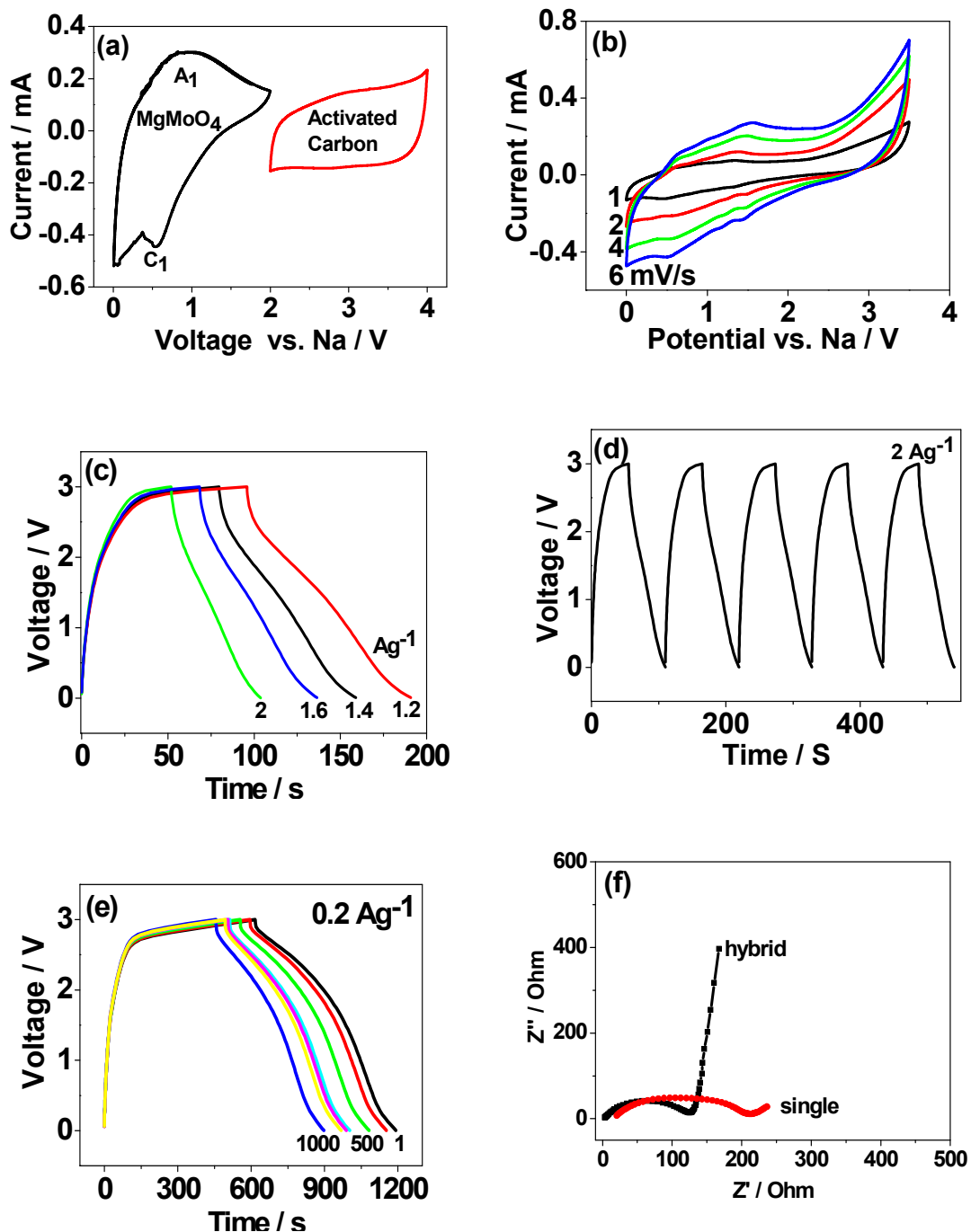


**Figure 7** (a) First CV curves (two-electrode configuration) of MgMoO<sub>4</sub> as negative compared with activated carbon as positive electrode versus metallic sodium in non-aqueous 1M NaClO<sub>4</sub> in EC: DMC: FEC (88:10:2) electrolyte. Hybrid cell (two-electrode configuration) (b) CV and (c) charge-discharge curves of supercapacitor comprising AC || MgMoO<sub>4</sub> in non-aqueous electrolyte. Both CV and charge-discharge curves show pseudocapacitive behaviour, (c-d) charge-discharge curves for consecutive cycles (f) Nyquist plot comparing the impedance in high frequency region and capacitive behaviour in low frequency region for (a) single and (b) hybrid cell. Sweep rates and cycles numbers are indicated in the respective figures.

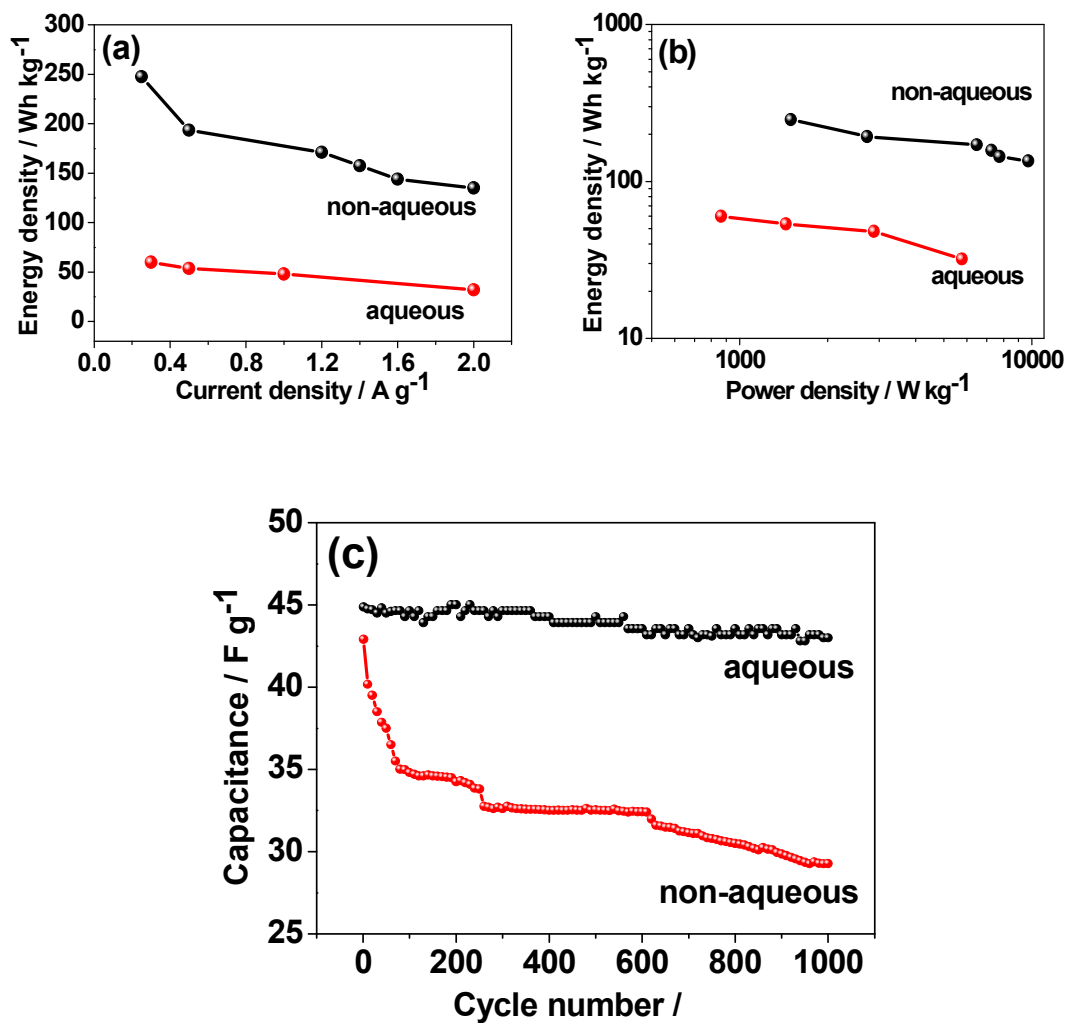


**Figure 8** Power performance characteristics of hybrid supercapacitor AC || MgMoO<sub>4</sub> (a) energy density plot, (b) Ragone plot, and (c) cycling stability in aqueous and non-aqueous electrolytes.



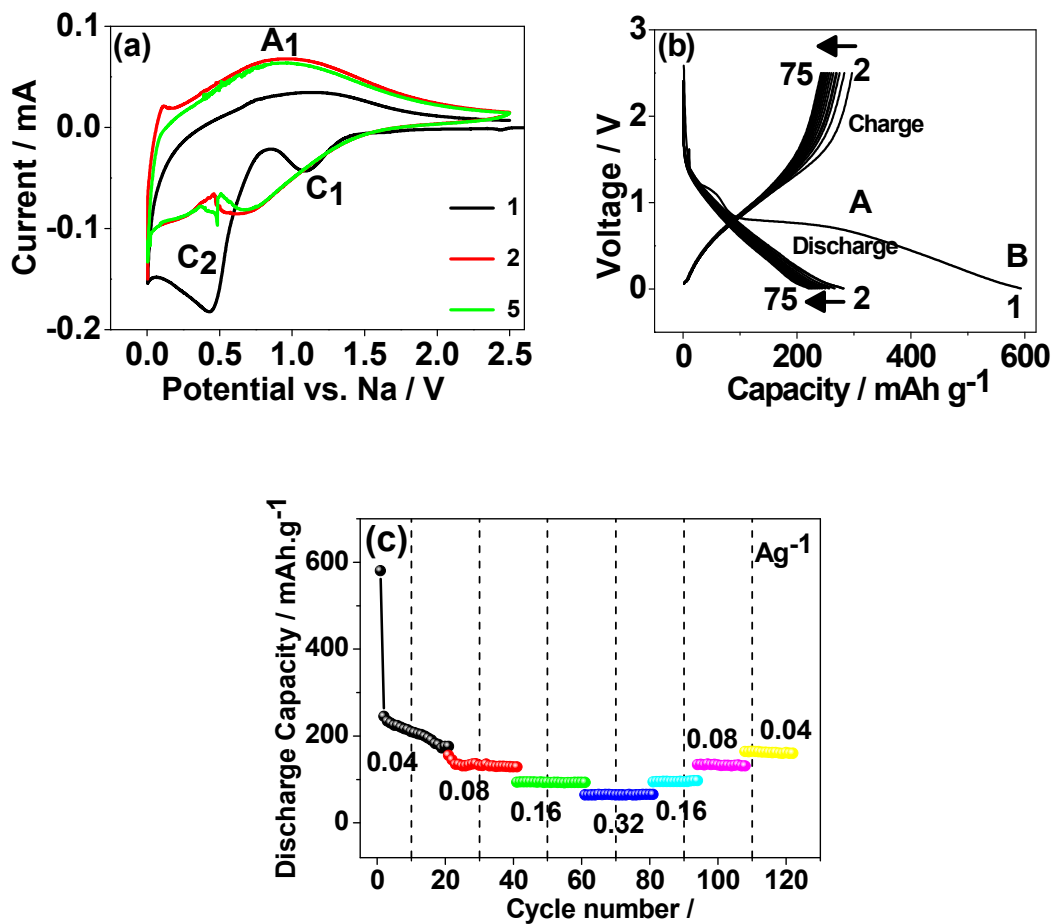


**Figure 9** (a) First five CV curves (two-cell configuration) of MgMoO<sub>4</sub> versus metallic sodium in non-aqueous 1M NaClO<sub>4</sub> in EC: DMC: FEC (88:10:2) electrolyte. (b) Charge-discharge behaviour, and (c) rate capability of sodium battery (Na || MgMoO<sub>4</sub>). Cycle numbers and current rates are indicated in the respective figures. The letters C<sub>1</sub>, C<sub>2</sub> and A<sub>1</sub> refers to reduction and oxidation peaks, respectively. The term “A” and “B” are boundary markings for the products formed during discharge, the region “A” is reversible.

## **New insights into the electrochemistry of magnesium molybdate hierarchical architectures for high performance sodium devices**

**<sup>1,2</sup>Manickam Minakshi\*, <sup>3</sup>David R.G. Mitchell, <sup>2</sup>Anji Reddy Munnangi, <sup>4</sup>Anders J. Barlow and <sup>2</sup>Maximilian Fichtner\***

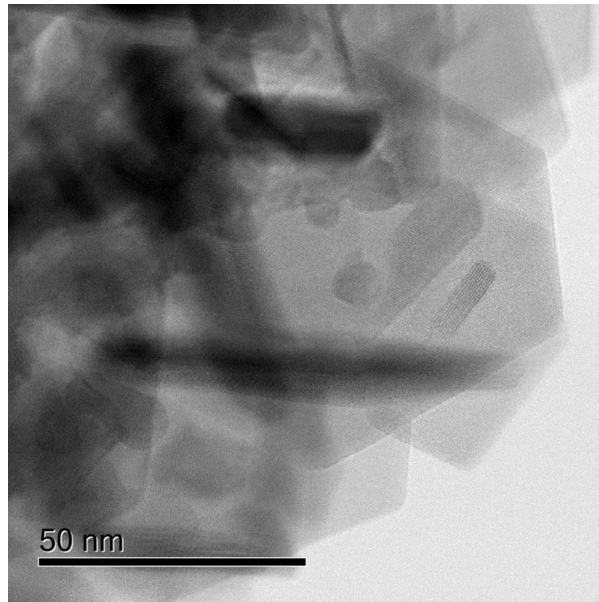
*<sup>1</sup>School of Engineering and Information Technology, Murdoch University, WA 6150, Australia*

*<sup>2</sup>Helmholtz Institute Ulm for Electrochemical Energy Storage (HIU), Ulm 89081, Germany*

*<sup>3</sup>Electron Microscopy Centre, Australian Institute for Innovative Materials, Innovation Campus, University of Wollongong, North Wollongong, NSW 2500, Australia*

*<sup>4</sup>Centre for Materials and Surface Science, La Trobe University, Bundoora, VIC 3086, Australia*

### **Table of Content (ToC)**



- Hierarchical plate-like magnesium molybdate anode for sodium devices storing energy with high rate performance and excellent capacity retention